NANO · MICRO small
www.small-journal.com

Self-Catalytic Ternary Compounds for Efficient Synthesis of High-Quality Boron Nitride Nanotubes

Nanyang Wang, Liping Ding, Taotao Li, Kai Zhang, Liyun Wu, Zhengyang Zhou, Qian He, Xuhua He, Xuebin Wang, Yue Hu, Feng Ding,* Jin Zhang,* and Yagang Yao**

The large-scale synthesis of high-quality boron nitride nanotubes (BNNTs) has attracted considerable interests due to their applications in nanocomposites, thermal management, and so on. Despite decades of development, efficient preparation of high-quality BNNTs, which relies on the effective design of precursors and catalysts and deep insights into the catalytic mechanisms, is still urgently needed. Here, a self-catalytic process is designed to grow high-quality BNNTs using ternary W–B–Li compounds. W–B–Li compounds provide boron source and catalyst for BNNTs growth. High-quality BNNTs are successfully obtained via this approach. Density functional theory-based molecular dynamics (DFT-MD) simulations demonstrate that the Li intercalation into the lattice of W_2B_5 promotes the formation of W–B–Li liquid and facilitates the compound evaporation for efficient BNNTs growth. This work demonstrates a high-efficient self-catalytic growth of high-quality BNNTs via ternary W–B–Li compounds, providing a new understanding of high-quality BNNTs growth.

1. Introduction

As a typical one-dimensional nanomaterial, boron nitride nanotubes (BNNTs) possess similar structures to carbon nanotubes (CNTs), by replacing C atoms with B and N elements periodically. Such an atomic substitution generates numerous distinct physical and chemical properties from CNTs, such as a large and uniform band gap (≈5.5 eV) nearly independent of the diameter and chirality, excellent electric insulativity,[1] high oxidation resistance up to 800 °C,[2] strong deep-ultra-violet light-emission,[3] high thermal conductivity,[4] neutron absorption,[5] etc. It is well known that the main synthesis methods of BNNTs include arc discharge,[6,7] plasma jet method,[8–10] laser heating,[11,12] ball-milling and annealing,[13,14] and chemical vapor deposition (CVD),[15,16] among which CVD is considered as a promising method to realize the low-cost batch preparation of BNNTs. Various precursors and catalysts were developed to fabricate BNNTs via the CVD method. The vapor-liquid-solid (VLS) growth, that the vapor precursors react with a liquid catalyst droplet and form the solid materials at the surface of the liquid catalyst,[17] is the generally accepted mechanism of BNNTs growth. However, the principles of designing the precursors and catalysts and their interdependent catalytic mechanisms are still blurred.[18–21] Therefore, it is necessary to deeply understand the growth mechanism of BNNTs, and to guide the development of novel precursors and catalysts to efficiently catalyze high-quality BNNTs growth.

Transition metals, such as tungsten,[22] hafnium,[23] and zirconium,[24] were proved to be effective catalysts for high-quality BNNTs growth at temperatures high up to 4000 K, by forming metal borides as liquid catalysts. But these metals and metal borides cannot be used in BNNTs CVD growth unless novel strategies to greatly lower their melting points.

In this work, we successfully introduce Li into the W-B compounds to lower the melting point of ternary W–B–Li compounds to satisfy the requirement for VLS high-quality BNNTs fabrication. We demonstrate the high growth efficiency of a W_2B_5/Li group and then extended it to other 6 groups of W–B–Li ternary compounds. The robust results undoubtedly confirm the high efficiency of the ternary W–B–Li compounds. The mechanism analysis shows that the W–B–Li compounds form low-melting eutectic liquid and evaporate into droplets

N. Wang, T. Li, K. Zhang, L. Wu, Z. Zhou, Q. He, X. He, X. Wang, Y. Yao
National Laboratory of Solid State Microstructures
College of Engineering and Applied Sciences
Jiangsu Key Laboratory of Artificial Functional Materials
Collaborative Innovation Center of Advanced Microstructures
Nanjing University
Nanjing 210023, China
E-mail: ygyao2018@nju.edu.cn

L. Ding
School of Electronic Information and Artificial Intelligence
Shaanxi University of Science & Technology
Xi'an 710021, China

Y. Hu
Key Laboratory of Carbon Materials of Zhejiang Province
College of Chemistry and Materials Engineering
Wenzhou University
Wenzhou 325000, China
E-mail: yuehu@wzu.edu.cnd

F. Ding
Center for Multidimensional Carbon Materials
Institute for Basic Science
Ulsan 44919, South Korea
E-mail: f.ding@unist.ac.kr

J. Zhang
College of Chemical and Molecular Engineering
Peking University
Beijing 100871, China
E-mail: jinzhang@pku.edu.cn

The ORCID identification number(s) for the author(s) of this article can be found under https://doi.org/10.1002/smll.202206933.

DOI: 10.1002/smll.202206933

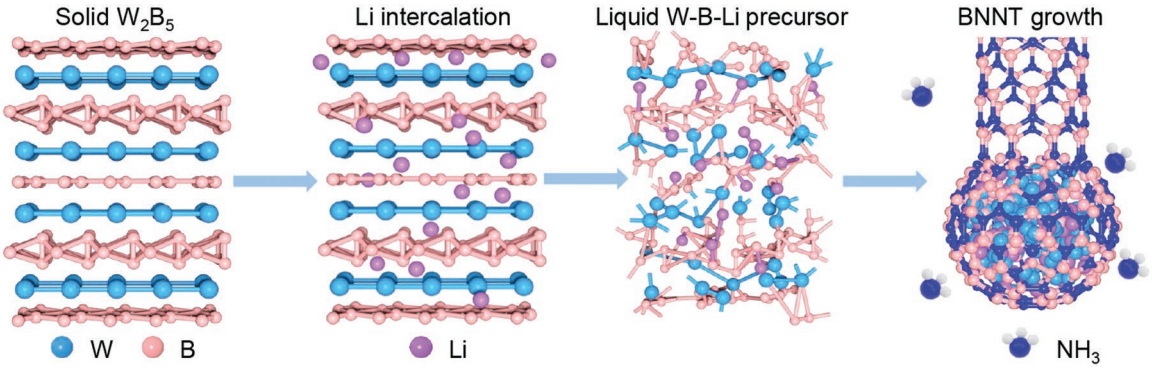

Scheme 1. Synthetic route to the BNNTs.

on a substrate to self-catalyze growth of BNNTs. As an example of applications, we have shown that the average thermal conductivity of the polyvinyl alcohol (PVA)/BNNT composite film with 13.8 wt.% BNNTs is 9.5 W m^{-1} K^{-1}, approximately 47.5 times higher than that of pure PVA. Infrared thermal imaging and thermal conductivity analysis of PVA/BNNT composite film show that the BNNTs prepared by this method have high thermal conductivity. Our study brings a new vision for precursor and catalyst design, a deep insight into the mechanism understanding, and a huge promotion of high-quality BNNTs fabrication.

2. Results and Discussion

The formation of W–B–Li compounds and BNNTs growth mechanism are schematically shown in **Scheme 1**. The solid tungsten boride, such as W_2B_5 has a high melting point up to 2365 °C, which was not applicable for the CVD growth of BNNTs (Figure S1c, Supporting Information). When annealed with Li at elevated temperatures, the Li atoms intercalate into the lattice of W_2B_5 and form a liquid compound, which evaporates and boosts the growth of BNNTs via a VLS mechanism.

Experimentally, a straightforward compound group – W_2B_5/Li – was employed and investigated. W_2B_5 and Li were mixed and put in a crucible. A substrate was placed on the top of the crucial and the whole system was annealed in an NH_3 atmosphere. After synthesis, a large number of snow-white products can be observed on the substrate, as shown in **Figure 1**a. The detailed morphology of the product was examined by scanning electron microscopy (SEM). As shown in Figure 1b,c, BNNTs longer than 20 µm are seen stacked together, and no impurities are observed. Transmission electron microscopy (TEM) investigations clearly present the hollow structure of a cylindrical and the diameter is found to be ≈15 nm (Figure 1d–f).[25–27] The diameter distribution of 50 BNNTs shows that the diameter of the tube is about 28 nm (Figure S2, Supporting Information). The selected area electron diffraction (SAED) pattern of BNNTs demonstrates the high crystallinity of the as-grown BNNTs (the inset of Figure 1d). High-resolution TEM (HRTEM) images show the walls are high-crystallized with an identical lattice spacing of 0.34 nm, corresponding to the (002) crystal plane of h-BN (Figure 1f).[28]

X-ray photoelectron spectroscopy (XPS), Raman spectroscopy, X-ray diffraction (XRD), and Fourier transform infrared spectroscopy (FTIR) were applied to further confirm the chemical components, purity, and crystallinity of the product. Figure 1g shows that the sample surface consists of B and N with binding energies of B 1s and N 1s of 190.6 and 398.2 eV, respectively, indicating the formation of BN.[29,30] The quantification of the peak intensities reveals that the atomic ratio of B and N is about 1:1, which agrees well with the composition of BNNT. The Raman spectrum also shows an intense peak at 1367 cm^{-1} attributed to the high-frequency interlayer E_{2g} vibration mode of h-BN. The half-width of the peak 13.9 cm^{-1} shows that high crystallinity of BNNTs as that observed in the TEM images (Figure 1h).[31–33] XRD characterization was carried out on the BNNTs as shown in Figure 1i. The peaks of the (002), (100), (101), (102) (004), and (110) planes are the characteristic signals of h-BN, which are consistent with that listed in the JCPDS card (no. 34–0421). As described in Figure S3, Supporting Information, a representative FTIR spectrum of the synthesized BNNTs presents three peaks. The peak at 808 cm^{-1} was attributed to the B–N–B bending vibration mode parallel to the c-axis, and the peak at 1370 cm^{-1} was thought to have resulted from the B–N stretching vibration mode perpendicular to the c-axis. The two peaks can be observed in the FTIR spectra of all h-BN. While, the peak located at 1538 cm^{-1}, which was attributed to the stretching of the h-BN network along the tangential directions of the BNNTs, only appeared in the spectra of highly pure and crystalline BNNTs. The XRD pattern of the residue after growth shows that W_2B_5 was transformed into W and BN, and no other boron-containing compounds were produced in the reaction, indicating that the reaction was carried out completely (Figure S4, Supporting Information). The above results prove that the W_2B_5/Li is effective for the growth of BNNTs and W_2B_5/Li compound serves as both catalyst and boron source during BNNTs growth.

A series of controlled experiments demonstrate that any precursor group consisting only two of the three elements is less effective for BNNTs growth. Three control groups of precursors a) B/Li_2O, b) B/Li, and c) W_2B_5 been used as precursors for growing BNNTs. However, very few BNNTs are observed and large amounts of impurities, crude fibers, and nanosheets were obtained (Figure S1a-c, Supporting Information). In another group, B/Li (tungsten sheet as the substrate), large amount of high-quality BNNTs without obvious impurities were obtained

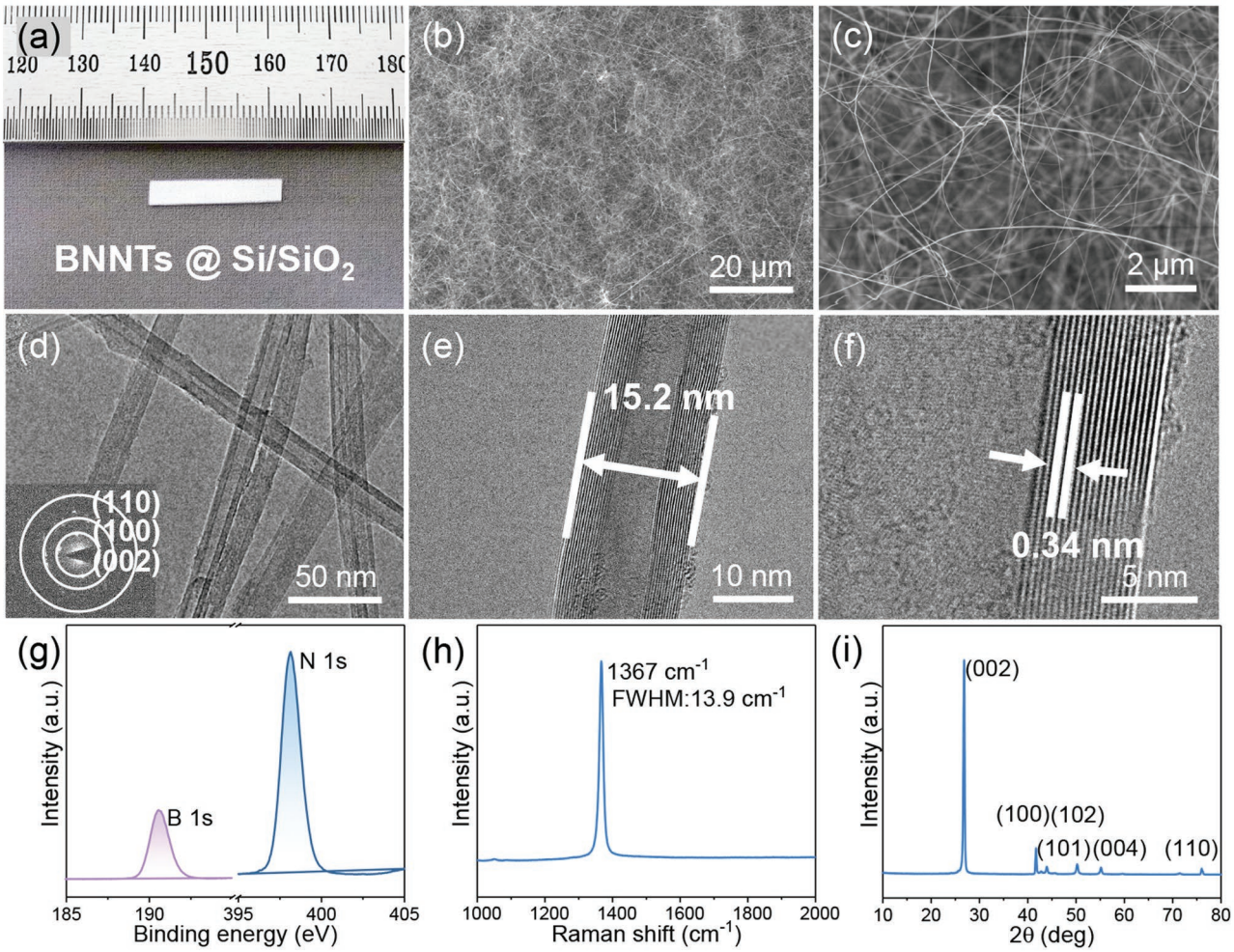

Figure 1. The preparation and characterization of the product formed from W_2B_5/Li. a) The optical photo of the substrate after growth. b,c) SEM images of the product. d,e) Representative TEM images of the product. The inset is the SAED pattern of the tube walls. f) HRTEM image of the tube walls. g–i) XPS, Raman spectra, and XRD pattern of the product: g) XPS spectrum, h) Raman spectrum, i) XRD pattern.

(Figure S1d, Supporting Information). These experiments prove the synergistic effect of the ternary compound.

To demonstrate the universality of the ternary W–B–Li compound, several groups of compounds including elementals, oxides, and salts were prepared for growing BNNTs. Six groups of compounds including W_2B_5/Li_2O, B/Li_2WO_4, $B/Li_2O/WO_3$, $B/Li_2O/W$, $B/Li/WO_3$, B/Li/W were respectively utilized for the BNNTs growth at the same condition. The results show that all compounds are available to get BNNTs without obvious impurities (Figure S5a-f, Supporting Information). The insets of them prove that all the products have cylindrical hollow structures with a diameter in the range of 14–30 nm. Raman characterization has a characteristic peak of h-BN at 1367 cm^{-1} (Figure S5g, Supporting Information). XPS spectra show that the products have B–N bonding (Figure S5h-i, Supporting Information), which further guarantees the chemical composition of the products is BN. When B/Li_2WO_4 (molar ratio = 5:1-7:1) were used as a compound, BNNTs can be obtained at 1100–1300 °C (Figure S6, Supporting Information), which indicates that the synergistic catalysis in liquid W–B–Li reduces the growth temperature.[34,35] BNNTs can be obtained by all the compounds containing W, B, and Li. The BNNTs obtained in this work are of higher quality compared to the results in the literature for the growth of BNNTs from metal borides (Table S1, Supporting Information).[22,23,36–39]

We demonstrate that the formation of liquid W–B–Li is critical for BNNTs growth. To confirm this, the above 7 groups of compounds were annealed following the growth procedure under Ar atmosphere without the introduction of NH_3. The obtained products were analyzed by SEM, TEM, XPS, XRD, and electron energy loss spectroscopy (EELS). SEM image shows that spherical particles were observed on the substrate, and elemental analysis reveals that the particles contained W and B, indicating the melting and evaporation of the W–B–Li compound (**Figure 2**a left, Figure S7a, Supporting Information). When using substrates with different properties, the results remain the same as those for Si/SiO_2 substrate, proving that the substrate does not affect the growth of BNNTs (Figure S7b-f, Supporting Information). XRD results show that W_2B_5 phase is the main product of all the annealing products. Only the annealing product of $B/Li/WO_3$ contains a small number of WB_4 (Figure 2b). The as-annealed particles are heated again

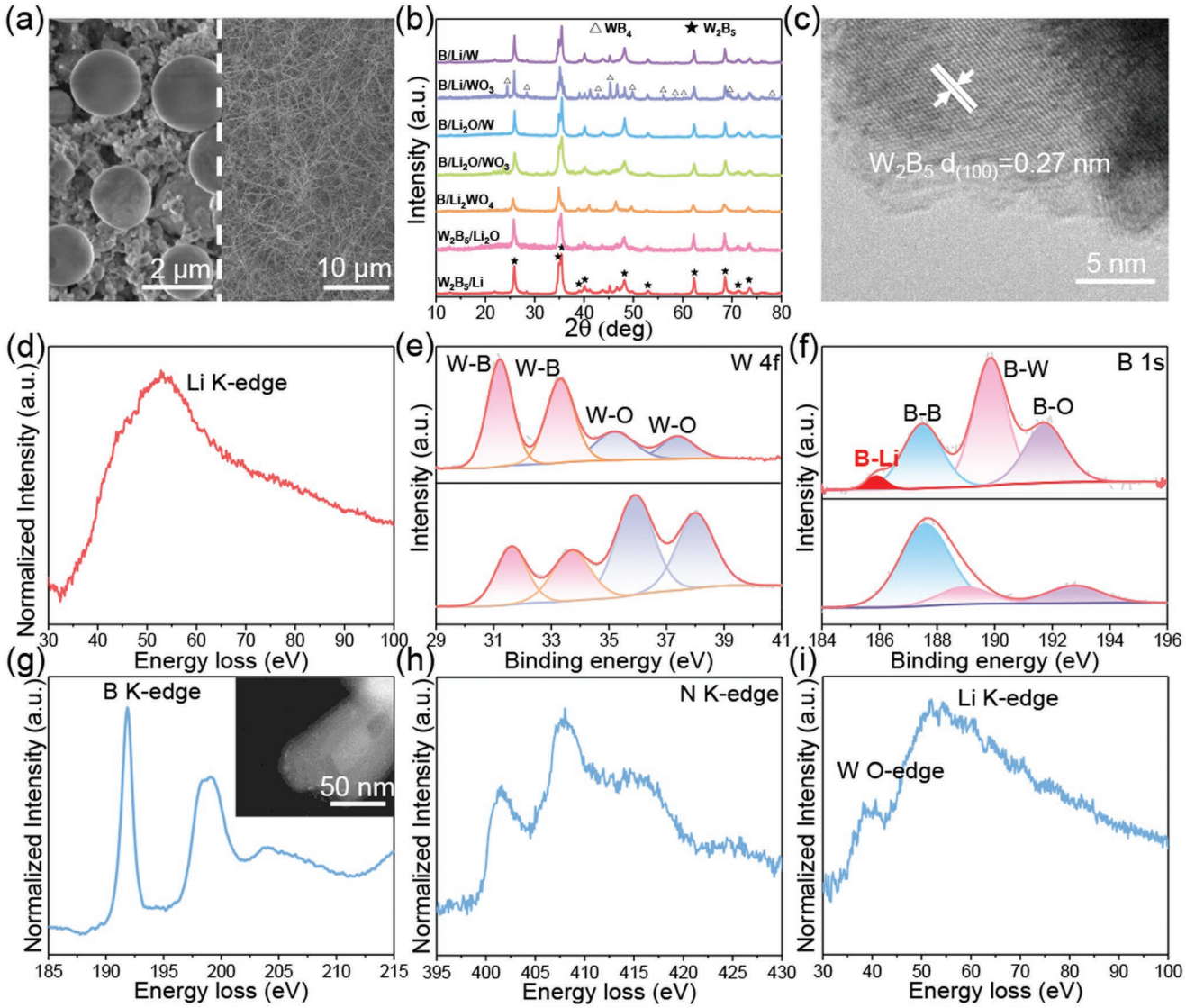

Figure 2. Study on the formation of liquid W–B–Li compound and catalytic growth of BNNTs. a) SEM image of the particles on the substrate and particles grown under ammonia. b) XRD of annealed products of different compounds. c) HRTEM image of W_2B_5/Li annealing product. d) EELS of the W_2B_5/Li annealing product. e,f) XPS spectra of W_2B_5 and W_2B_5/Li annealing product, e) W 4f, f) B 1s. g–i) EELS of the nanoparticle at BNNT end, the inset is the scanning transmission electron microscopy (STEM) image of the BNNT end.

in NH_3 atmosphere following the growth procedure, large amount of BNNTs can be obtained (Figure 2a right). These results suggest that W_2B_5/Li is the actual substance that contribute to BNNTs growth among these compounds. It is a reasonable speculation that Li intercalates into W_2B_5, promotes the melting of W–B–Li compounds and the evaporation of W–B–Li compounds at elevated temperature. TEM result demonstrates that W_2B_5 (100) crystal plane lattice spacing is 0.27 nm, which is larger than the theoretical 0.26 nm (Figure 2c),[40] indicating the intercalation of Li into the W_2B_5 lattice. Furthermore, the EELS and XPS spectra confirm the existence of Li in the W_2B_5 lattice. Figure 2d shows that the Ar-annealed product formed from the W_2B_5/Li contains Li. Figure 2e and f show the XPS peaks of W 4f and B 1s in pure W_2B_5 (the bottom) and the Ar-annealed W_2B_5/Li (the top), respectively. As for W_2B_5, the W 4f peaks assignments belong to the W–B and W–O bond, and the peaks of B 1s are attributed to the B–O, B–W, B–B bond.[41,42] The formation of the W–O and B–O bond is due to the adsorbed oxygen in the air.[42] In contrast, Ar-annealed W_2B_5/Li precursor shows all the peaks corresponding to W_2B_5, except that a B–Li bond peak at 185.9 eV is observed (Figure 2f),[43] which confirms the Li entering into the W_2B_5 lattice and explains the difference in growth efficiency between W_2B_5 and W_2B_5/Li compound. In addition, a comparison between two samples found that the peaks of the Ar-annealed W_2B_5/Li shifted to lower energy, which was due to the lower electronegativity of Li than that of W and B.[44]

To further study the growth mechanism of BNNTs growth catalyzed by the W–B–Li compounds, we performed compositional characterizations on the catalyst particles found at the end

of the nanotube, and confirmed the composition of W–B–Li. As shown in Figure 2g, a BNNT end has an encapsulated nanoparticle. EELS result shows that the particle contains the elements of W, Li, B, and N,[45–47] proving that W–B–Li synergistically catalyze the growth of BNNT (Figure 2g–i). Therefore, W, B, and Li are essential for catalyzing BNNTs growth. Li enters the lattice of the layered W_2B_5, which leads to a liquid ternary W–B–Li compound for the efficient growth of BNNTs.

Based on first-principle calculations and molecular dynamic simulations, we explored how the liquid W–B–Li compound forms and boosts the BNNT growth. The liquefaction of W_2B_5 induced by doping with different ratios of Li atoms ($Li_xW_2B_5$, x = 0.25, 0.75, 1, and 2) was explored by the density functional theory-based molecular dynamic (DFT-MD) simulations. In these simulations, the molar ratio of LiW_2B_5 is the same as that of the compound used in our experiment. As shown in **Figure 3**a and Figure S8a, Supporting Information, Li atoms are intercalated into the lattice gap of W_2B_5 and tend to react with B atoms nearby. The interaction between B and Li atoms leads to the destruction of W_2B_5 crystal structure at large Li ratio (≥0.75). Formation energy calculations also show that the intercalation of the W_2B_5 with large number of Li atoms tend to reconstruct the compounds with different structures (Figure S8b, Supporting Information). It is well known that Root Mean Square Deviation (RMSD) can be used to estimate the melting of a system, including clusters,[48,49] alloys and so on.[50–52] As shown in Figure 3b and Figure S8c,d, Supporting Information, we have calculated RMSD for $Li_xW_2B_5$ (x = 0, 0.25, and 1), respectively. The RMSD results show that LiW_2B_5 ternary system melts at 1400 K and the melting point of the W–B–Li ternary

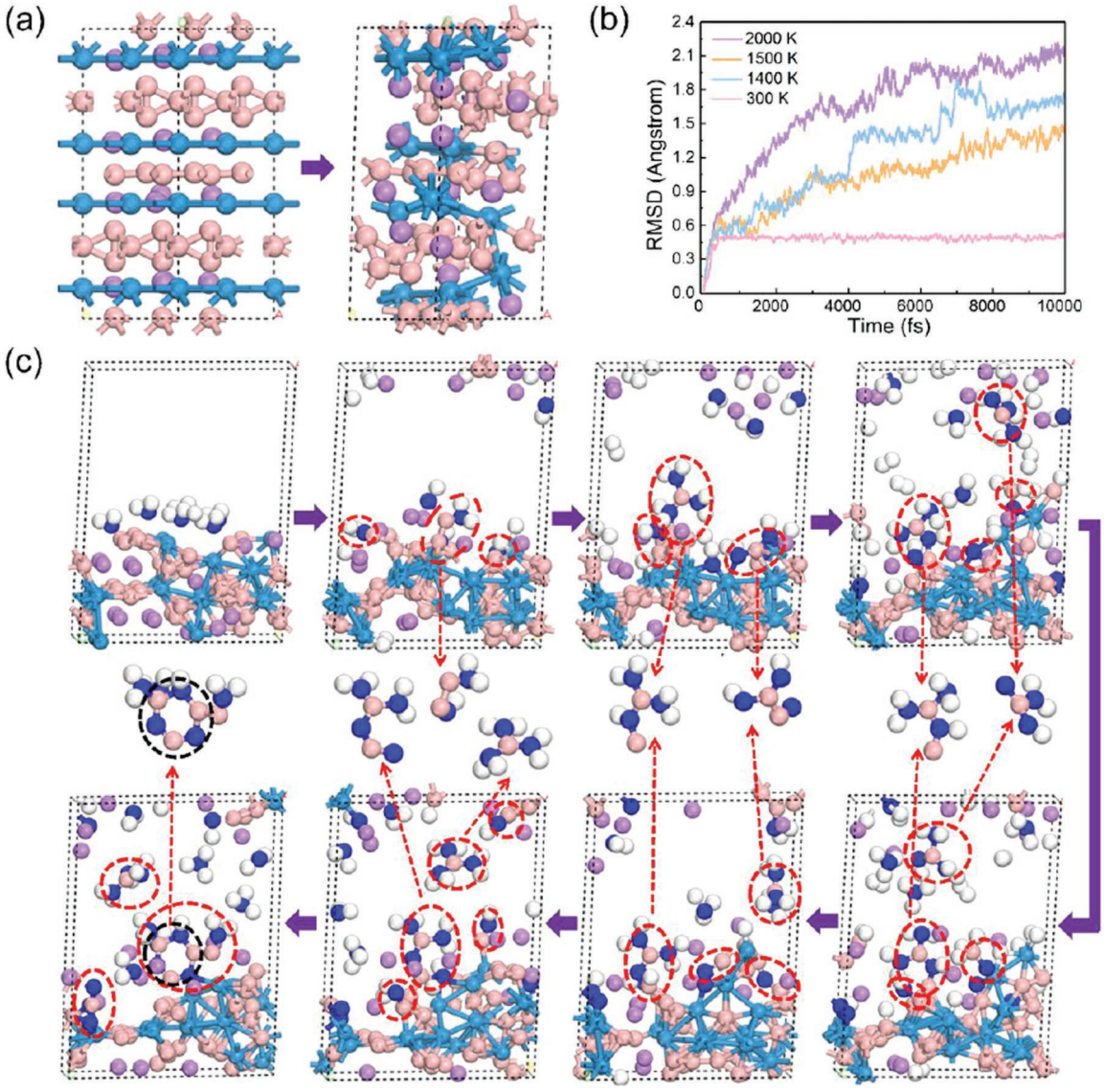

Figure 3. Li doping induced liquefaction of W_2B_5 and the nucleation of BNNT on liquid W–B–Li. a) The structures of LiW_2B_5 before and after relaxation at ambient conditions. b) The RMSD of the atoms of LiW_2B_5 during MD simulations at different temperatures. c) Continuous adding of NH_3 molecules onto the surface of liquid W–B–Li system leading to the nucleation of BNNT as observed in MD simulation at 1400 K. Pink: B, light blue: W, purple: Li, dark blue: N, white: H.

system can be controlled by adjusting the amount of Li. Here, we take the growth of BNNT catalyzed by LiW_2B_5 as an example to explore the catalytic growth of BNNT. Some snapshots taken during the MD trajectory are presented in Figure 3c, and more details are shown in Figures S9 and S10, Supporting Information. By continuously adding NH_3 molecules to the surface of liquid LiW_2B_5, the nucleation of a B_3N_3 ring (black circle) was observed in the MD simulation at 1400 K. In addition, at the early stage of nucleation, many small $B_xN_yH_z$ clusters, such as B-NH_x, H_xN-B-NH_x and Y-shaped B-NH_x units (red circles) can be clearly seen, suggesting that liquid W–B–Li can promote the formation of h-BN on its surface. Although we cannot simulate the formation of a BNNT due to the huge computational costs of the DFT-MD, these observations during the very short period of DFT-MD trajectories clearly showed that h-BN nucleation on liquid W–B–Li compound is preferred, thus the speculated VLS mechanism of BNNT growth is reasonable.

BNNTs can be widely used in thermal conductivity composites, the heat dissipation tests and thermal conductivity analysis were performed to demonstrate the heat-conduction property of the as-grown BNNTs. The PVA/BNNT composite film was prepared with a solution method. The heat dissipation tests were conducted by wrapping compacted composite film around a radiator to dissipate the heat generated by LED lights over identical operation times, then directly observing the change in surface temperature using an infrared thermal imager. The PVA/BNNT composite film exhibited a lower surface temperature than the film of pure PVA during the 70 s operation of the LED lights, indicating the better heat-dissipation performance of the PVA/BNNT composite film due to its higher thermal conductivity (**Figure 4**). The in-plane thermal conductivity analysis was further performed to quantify the heat conduction of the PVA/BNNT composite film. The average thermal conductivity of the PVA/BNNT composite film with 13.8 wt% BNNTs is determined to be 9.5 W m^{-1} K^{-1}. Compared with other BNNT-based polymer composites, the composite film here has higher thermal conductivity (Table S2, Supporting Information).[53–56] The theoretical thermal conductivity of pure PVA is 0.2 W m^{-1} K^{-1}, and the thermal conductivity of the PVA/BNNT composite film is about 47.5 times higher than that of pure PVA. Infrared thermal imaging and in-plane thermal conductivity of the PVA/BNNT composite film indicate that the as-prepared BNNTs have high thermal conductivity. In addition, as-prepared BNNTs also have high-temperature oxidation resistance up to 800 °C (Figure S11, Supporting Information).

3. Conclusion

In conclusion, a series of self-catalytic ternary W–B–Li compounds have successfully developed to synthesize high-quality BNNTs efficiently. Together with computational studies, we have shown that intercalation of Li into the lattice of W_2B_5 leads to the liquefaction of W_2B_5 and the eutectic liquid of W–B–Li compounds boosts the growth of BNNTs. The mechanism investigation suggests that W–B–Li serves as the concerted catalysts and boron source. In addition, the average thermal conductivity of the PVA/BNNT composite film with 13.8 wt% BNNTs is determined to be 9.5 W m^{-1} K^{-1}, approximately 47.5 times higher than that of pure PVA, indicating that the as-prepared BNNTs have high thermal conductivity. This self-catalytic ternary compound has guiding significance for the development of novel catalysts and growth mechanism. In addition, this design method enables more high melting point metals to liquefy in CVD system and can be used to catalyze the formation of other one-dimensional nanomaterials.

4. Experimental Section

Materials Preparations: All reagents were commercially available and used without further purification. Tungsten boride (W_2B_5, 99.4%) and lithium tungstate (Li_2WO_4, 99%) were purchased from Alfa Aesar (China) Chemical Co., Ltd. Amorphous boron powder (B, 99.99%), tungsten (W, 99.99%), and polyvinyl alcohol (PVA) were provided by

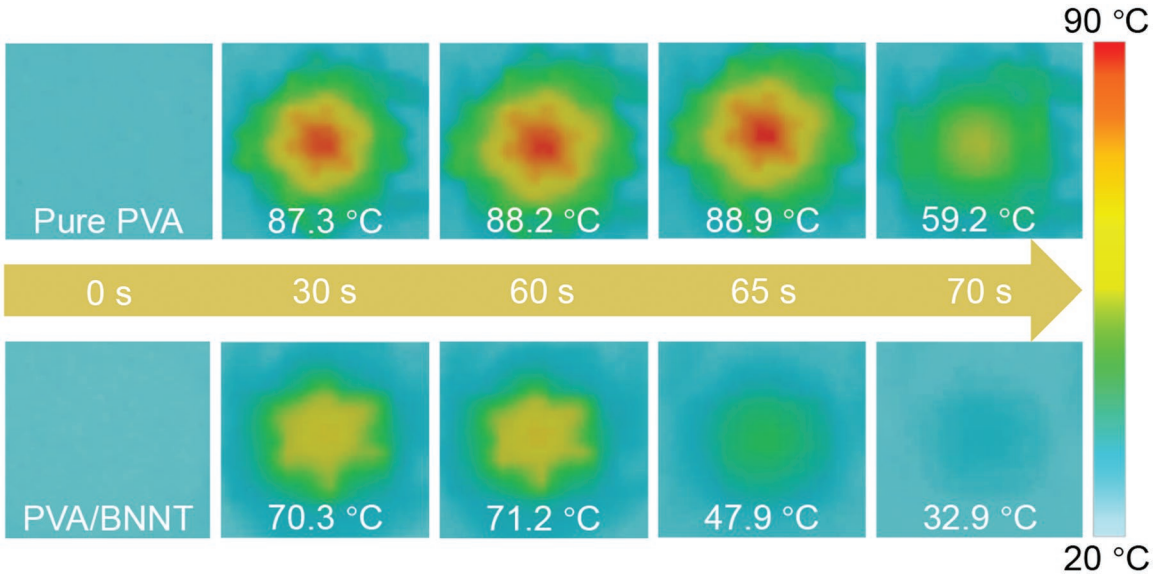

Figure 4. Infrared thermal images of the pure PVA and PVA/BNNT composite film.

Aladdin Chemistry Co., China. Lithium oxide (Li_2O, 99.99%) and Tungsten oxide (WO_3, 99%) were purchased from Shanghai McLean Biochemical Technology Co., Ltd. and 3A (Anhui Zesheng Technology Co., Ltd.), respectively. Lithium was provided by Tianjin Zhongneng Co., Ltd.

Preparation of BNNTs: BNNTs were synthesized by using an ordinary horizontal tube furnace (Hefei Keijing GSL-1700). The mixture of W_2B_5 and lithium (molar ratio W_2B_5: Li = 1:1) was loaded into a boron nitride crucible at the center of an Al_2O_3 tube (diameter of 60 cm, length of 100 cm) and Si/SiO_2 substrate upside down on the boat, which was located in the horizontal tube furnace. It was annealed under NH_3 at1210 °C for 2 h. The temperature was increased at a rate of 10 °C min^{-1} to 1210 °C and was maintained at that temperature for 2 h, then cool down at a rate of 10 °C min^{-1}. During the heating and cooling process, argon flowed at a rate of 200 standard cubic centimeters per minute (sccm). Ammonia flowed at a rate of 200 sccm when the temperature rose to 1210 °C. Finally, snow-white products were collected on the Si/SiO_2 substrate. The growth of BNNTs with several other precursors was also carried out under the above conditions.

Preparation of PVA/BNNT Composite Film: 1 g PVA was heated and dissolved in 20 ml H_2O. 0.0345 g of BNNTs was dispersed in a solution with a volume ratio of water and ethanol of 1:1, and sonicated for 30 min. Then BNNTs dispersion with 5 mL PVA solution was mixed and stirred for 4 h, transferred to a petri dish, evaporated to dryness at 70 °C to form a film.

Characterization: The products were characterized by scanning electron microscope (SEM, Hitachi SU-8100) and transmission electron microscopy (TEM) with the selected area electron diffraction (SAED) was acquired by an FEI TEC-NAI F30 (200 kV). Raman spectroscopy was collected over the spectral range of 1000–2000 cm^{-1} using LabRAM ARAMIS Raman confocal microscope (HORIBA JobinYvon) equipped with a wavelength of 532 nm. The crystal structure was characterized by X-ray diffraction (XRD, D8 Advance, Bruker AXS). XPS analysis was performed using an ESCALAB 250Xi system from Thermo Scientific. The in-plane thermal diffusivities (α) of the PVA/BNNT composite film was detected with a laser-flash diffusivity instrument (LFA 447, NETZSCH). The thermal conductivity was calculated from the equation: $\kappa = \alpha \times \rho \times c$, where α is the thermal diffusivity, ρ is the density, and c is the specific heat of the composite film.

DFT-MD Calculations: All the structural optimization was performed by density functional theory (DFT) calculations as implemented in the Vienna Ab initio Simulation Package with the interaction of valence electrons-ion cores described by projector-augmented wave method. The Perdew—Burke–Ernzerhof exchange-correlation functional was used for the interaction between valence electrons. It was used a plane wave basis set with a cutoff energy of 450 eV in the calculations. All the structures were fully relaxed, and the convergence criteria for energy and force were set at 10^{-5} eV and 10^{-5} eV/Å, respectively. The DFT-MD (molecular dynamic) simulations employ an NPT ensemble and a 1.0 fs time step.

The formation energies (Figure S3b, Supporting Information) are calculated using the following formula:

$$E_f = \frac{E_{total} - n_W E_W - n_B E_B - n_{Li} E_{Li}}{(n_W + n_B + n_{Li})} \quad (1)$$

where E_{total} is the energy of system $Li_xW_2B_5$. $E_{w,}$ $E_{B,}$ and E_{Li} are the energies of the W, B, and Li in their bulks, respectively. n_W, $n_{B,}$ and n_{Li} are the numbers of W, B, and Li atoms in systems, respectively.

To further illustrate that Li atoms doping can break the crystal structure of W_2B_5, it was calculated the root mean square deviation (RMSD) of $Li_xW_2B_5$ systems using the formula:

$$RMSD = \sqrt{\frac{\sum_{i=1}^{N_{atom}} \left(r_i(t_1) - r_i(t_2)\right)^2}{N_{atom}}} \quad (2)$$

where $r_i(t_1)$ and $r_i(t_2)$ are the positions of any atom i in the system at the time of t_1 and t_2, respectively. N_{atom} is the total number of atoms.

Supporting Information

Supporting Information is available from the Wiley Online Library or from the author.

Acknowledgements

N.W., L.D., and T.L. contributed equally to this work. This work was supported by the National Natural Science Foundation of China (No. 51972162), the Institute for Basic Science (IBS-R019-D1) of South Korea and computational resources from CMCM, IBS. [Correction added after publication 5 April 2023: Affiliations and Acknowledgements were corrected.]

Conflict of Interest

The authors declare no conflict of interest.

Data Availability Statement

The data that support the findings of this study are available in the supplementary material of this article.

Keywords

boron nitride nanotubes, self-catalysis, thermal conductivity, vapor-liquid-solid growth, W–B–Li compounds

Received: November 9, 2022
Revised: December 11, 2022
Published online: January 11, 2023

[1] X. Blase, A. Rubio, S. Louie, M. Cohen, *Europhys. Lett.* **1994**, *28*, 335.
[2] L. Li, J. Cervenka, K. Watanabe, T. Taniguchi, Y. Chen, *ACS Nano* **2014**, *8*, 1457.
[3] Y. Kubota, K. Watanabe, O. Tsuda, T. Taniguchi, *Science* **2007**, *317*, 932.
[4] C. Zhi, Y. Xu, Y. Bando, D. Golberg, *ACS Nano* **2011**, *5*, 6571.
[5] C. Harrison, S. Weaver, C. Bertelsen, E. Burgett, N. Hertel, E. Grulke, *J. Appl. Polym. Sci.* **2008**, *109*, 2529.
[6] J. Cumings, A. Zettl, *Chem. Phys. Lett.* **2000**, *316*, 211.
[7] S. Biswajit, H. Ko, Y. Yeh, F. Martelli, I. Kaganovich, Y. Raitses, R. Car, *Nanoscale* **2018**, *10*, 22223.
[8] Y. Shimizu, Y. Moriyoshi, H. Tanaka, S. Komatsu, *Appl. Phys. Lett.* **1999**, *75*, 929.
[9] K. Kim, C. Kingston, A. Hrdina, M. Jakubinek, J. Guan, M. Plunkett, B. Simard, *ACS Nano* **2014**, *8*, 6211.
[10] M. Kim, Y. Lee, J. Oh, S. Hong, B. Min, T. Kim, S. Choi, *Chem. Eng. J.* **2020**, *395*, 125148.
[11] H. Cho, J. Kim, J. Hwang, C. Kim, S. Jang, C. Park, H. Lee, M. Kim, *Sci. Rep.* **2020**, *10*, 7416.
[12] M. Smith, K. Jordan, C. Park, J. Kim, P. Lillehei, R. Crooks, *Nanotechnology* **2009**, *20*, 505604.
[13] Y. Li, J. Zhou, K. Zhao, S. Tung, E. Schneider, *Mater. Lett.* **2009**, *63*, 1733.
[14] S. E. , R. Geng, Z. Zhu, L. Xie, W. Lu, C. Li, Y. Yao, *Ceram. Int.* **2018**, *44*, 22794.
[15] M. Baysal, K. Bilge, M. Yildizhan, Y. Yorulmaz, C. Oncel, M. Papila, Y. Yurum, *Nanoscale* **2018**, *10*, 4658.

[16] Z. Chen, J. Zou, Q. Liu, C. Sun, G. Liu, X. Yao, F. Li, B. Wu, X. Yuan, T. Sekiguchui, *ACS Nano* **2008**, *2*, 1523.
[17] T. Trentler, J. Timothy, Hickman, M. K. , *Science* **1995**, *270*, 1791.
[18] C. Tang, M. de la Chapelle, P. Li, Y. Liu, H. Dang, S. S. Fan, *Chem. Phys. Lett.* **2001**, *342*, 492.
[19] C. Tang, Y. Bando, T. Sato, K. Kurashima, *Chem. Commun.* **2002**, 1290.
[20] C. Zhi, Y. Bando, C. Tan, D. Golberg, *Solid State Commun.* **2005**, *135*, 67.
[21] J. Shrine, M. Nithya, A. Pandurangan, *J. Nanosci. Nanotechnol.* **2012**, *12*, 3831.
[22] N. Chopra, R. Luyken, K. Cherrey, V. Crespi, M. Cohen, S. Louie, A. Zettl, *Science* **1995**, *269*, 966.
[23] Loiseau, F. W. , N. Demoncy, G. Hug, H. Pascard, *Phys. Rev. Lett.* **1996**, *76*, 4737.
[24] P. Gleize, M. Schouler, P. Gadelle, M. Caillet, *J. Mater. Sci. Lett.* **1994**, *29*, 1575.
[25] L. Li, X. Liu, L. Li, Y. Chen, *Microelectron. Eng.* **2013**, *110*, 256.
[26] H. Guo, Y. Xu, H. Chen, Z. Wang, X. Mao, G. Zhou, J. Zhang, S. Wang, *Materials* **2020**, *13*, 915.
[27] Z. Chen, J. Zou, F. Li, X. Zhi, G. Liu, D. Tang, D. Li, C. Liu, X. Ma, H. Cheng, G. Lu, Z. Zhang, *Adv. Funct. Mater.* **2007**, *17*, 3371.
[28] Z. Chen, J. Zou, G. Liu, F. Li, Y. Wang, L. Wang, X. Yuan, T. Sekiguchi, H. Chen, G. Liu, *ACS Nano* **2008**, *2*, 2183.
[29] Z. Liu, B. Yan, S. Meng, R. Liu, W. Lu, J. Sheng, Y. Yi, A. Lu, *Angew. Chem., Int. Ed.* **2021**, *60*, 19691.
[30] C. Marichy, V. Salles, X. Jaurand, A. Etiemble, T. Douillard, J. Faugier-Tovar, F. Cauwet, A. Brioude, *RSC Adv.* **2017**, *7*, 20709.
[31] L. Guo, R. Singh, *Physica E Low Dimens Syst Nanostruct* **2009**, *41*, 448.
[32] S. E. , L. Wu, C. Li, Z. Zhu, X. Long, R. Geng, J. Zhang, Z. Li, W. Lu, Y. Yao, *Nanoscale* **2018**, *10*, 13895.
[33] D. Golberg, Y. Bando, M. Eremets, K. Takemura, K. Kurashima, H. Yusa, *Appl. Phys. Lett.* **1996**, *69*, 2045.
[34] Y. Huang, J. Lin, C. Tang, Y. Bando, C. Zhi, T. Zhai, B. Dierre, T. Sekiguchi, D. Golberg, *Nanotechnology.* **2011**, *22*, 145602.
[35] M. He, A. Chernov, E. Obraztsova, H. Jiang, E. Kauppinen, J. Lehtonen, *Carbon* **2013**, *52*, 590.
[36] O. Lourie, C. Jones, B. Bartlett, P. Gibbons, R. Ruoff, W. Buhro, *Chem. Mater.* **2000**, *12*, 1808.
[37] K. Huo, Z. Hu, J. Fu, H. Xu, X. Wang, Y. Lu, *J. Phys. Chem. B* **2010**, *107*, 11316.
[38] J. Fu, Y. Lu, H. Xu, K. Huo, X. Wang, L. Li, Z. Hu, Y. Chen, *Nanotechnology* **2004**, *15*, 727.
[39] P. Ahmad, M. Khandaker, N. Muhammad, F. Rehman, G. Khan, A. Khan, Z. Ullah, M. Rehman, S. Ahmed, M. Gulzar, I. Din, S. Ahmed, H. Ali, N. Arshid, *Mater. Res. Bull.* **2018**, *98*, 235.
[40] B. Dai, X. Ding, X. Deng, J. Zhe, S. Ran, *Ceram. Int.* **2020**, *46*, 14469.
[41] M. Alishahi, S. Mirzaei, P. Soucek, L. Zabransky, V. Bursikova, M. Stupavska, V. Perina, K. Balazsi, Z. Czigany, P. Vasina, *Surf. Coat. 80 [Eighty], Annu. Natl. Tech. Semin., 11th* **2018**, *340*, 103.
[42] J. Pan, C. Zhen, L. Wang, G. Liu, H. Cheng, *Sci. Bull.* **2018**, *62*, 114.
[43] D. Hensley, S. Garofalini, *Appl. Surf. Sci.* **1994**, *81*, 331.
[44] T. Moscicki, R. Psiuk, H. Slominska, N. Levintant-Zayonts, D. Garbiec, M. Pisarek, P. Bazarnik, S. Nosewicz, J. Chrzanowska-Gizynska, *Surf. Coat. 80 [Eighty], Annu. Natl. Tech. Semin., 11th* **2020**, *390*, 125689.
[45] C. Tang, Y. Bando, T. Sato, *Appl. Phys. A* **2002**, *75*, 681.
[46] Y. Huang, Y. Bando, C. Tang, C. Zhi, T. Terao, B. Dierre, T. Sekiguchi, D. Golberg, *Nanotechnology* **2009**, *20*, 085705.
[47] W. Zhang, D. Seo, T. Chen, L. Wu, M. Topsakal, Y. Zhu, D. Lu, G. Ceder, F. Wang, *Science* **2020**, *367*, 1030.
[48] S. Dehghani, *J. Nano Res.* **2020**, *61*, 78.
[49] S. Sankaranarayanan, V. Bhethanabotla, B. Joseph, *Phys. Rev. B* **2005**, *71*, 195415.
[50] R. Subbaraman, S. Sankaranarayanan, *Phys. Rev. B* **2011**, *84*, 075434.
[51] R. McCormack, D. deFontaine, *Phys. Rev. B* **1996**, *54*, 9746.
[52] L. Xie, P. Brault, A. Thomann, J. Bauchire, *Appl. Surf. Sci.* **2013**, *285*, 810.
[53] C. Zhi, Y. Bando, T. Terao, C. Tang, H. Kuwahara, D. Golberg, *Adv. Funct. Mater.* **2009**, *19*, 1857.
[54] T. Terao, Y. Bando, M. Mitome, C. Zhi, C. Tang, D. Golberg, *J. Phys. Chem. C* **2009**,*113*, 13605.
[55] T. Terao, C. Zhi, Y. Bando, M. Mitome, C. Tang, D. Golberg, *J. Phys. Chem. C* **2010**, *114*, 4340.
[56] M. Wang, T. Zhang, D. Mao, Y. Yao, X. Zheng, L. Ren, Q. Cai, S. Mateti, L. Li, X. Zeng, G. Du, R. Sun, Y. Chen, J. Xu, C. Wong, *ACS Nano* **2019**, *13*, 7402.